PDA-BPs integrated mussel-inspired multifunctional hydrogel coating on PPENK implants for anti-tumor therapy, antibacterial infection and bone regeneration

Yizheng Li [a,b], Chengde Liu [a,b,**], Xitong Cheng [b], Jinyan Wang [b], Yue Pan [c], Cheng Liu [a], Shouhai Zhang [b], Xigao Jian [d,*]

[a] *State Key Laboratory of Fine Chemicals, Frontier Science Center for Smart Materials, School of Chemical Engineering, Dalian University of Technology, Dalian, 116024, China*
[b] *Department of Polymer Science and Engineering, Dalian University of Technology, Dalian, 116024, China*
[c] *State Key Laboratory of Fine Chemicals, Department of Pharmaceutical Sciences, School of Chemical Engineering, Dalian University of Technology, Dalian, 116024, China*
[d] *Liaoning Province Engineering Research Centre of High-Performance Resins, Dalian, 116024, China*

ARTICLE INFO

ABSTRACT

Currently, many cancer patients with bone defects are still threatened by tumor recurrence, postoperative bacterial infection, and massive bone loss. Many methods have been studied to endow bone implants with biocompatibility, but it is difficult to find an implant material that can simultaneously solve the problems of anticancer, antibacterial and bone promotion. Here, a multifunctional gelatin methacrylate/dopamine methacrylate adhesive hydrogel coating containing 2D black phosphorus (BP) nanoparticle protected by polydopamine (pBP) is prepared by photocrosslinking to modify the surface of poly (aryl ether nitrile ketone) containing phthalazinone (PPENK) implant. The multifunctional hydrogel coating works in conjunction with pBP, which can deliver drug through photothermal mediation and kill bacteria through photodynamic therapy at the initial phase followed by promotion of osteointegration. In this design, photothermal effect of pBP control the release of doxorubicin hydrochloride loaded via electrostatic attraction. Meanwhile, pBP can generate reactive oxygen species (ROS) to eliminate bacterial infection under 808 nm laser. In the slow degradation process, pBP not only effectively consumes excess ROS and avoid apoptosis induced by ROS in normal cells, but also degrade into PO_4^{3-} to promote osteogenesis. In summary, nanocomposite hydrogel coatings provide a promising strategy for treatment of cancer patients with bone defects.

1. Introduction

In China, about forty thousand people were diagnosed with primary osteosarcoma annually, and surgical excision was the most optimal method of treatment. However, the remaining tumor cells might re-emerge and proliferate, causing the cancer relapse [1]. Although traditional treatment methods such as chemotherapy could inhibit cancer cells, there were also various shortcomings, such as poor drug targeting, large toxic side effects and limited efficacy. Unfortunately, most of osteosarcoma was osteolytic and result in devastating bone loss [2].

What's more, the risk of bacterial infection associated with surgery reduced the osteogenic effect of implant materials in the body [3]. Hence, an optimal implant material for post-surgical tumor therapy should not only satisfy the needs of repairing bone defects, but also had various features such as removing the remaining tumor cells, avoiding bacterial infection, and accelerating bone tissue regeneration.

Lately, black phosphorus (BP), a novel 2D nano-material, has exhibited various unique characteristics, like a layer-dependent band gap from 0.3 eV to ≈2.0 eV [4] which lead to a broad absorption across the UV and IR regions [5,6]; A higher specific surface area which could
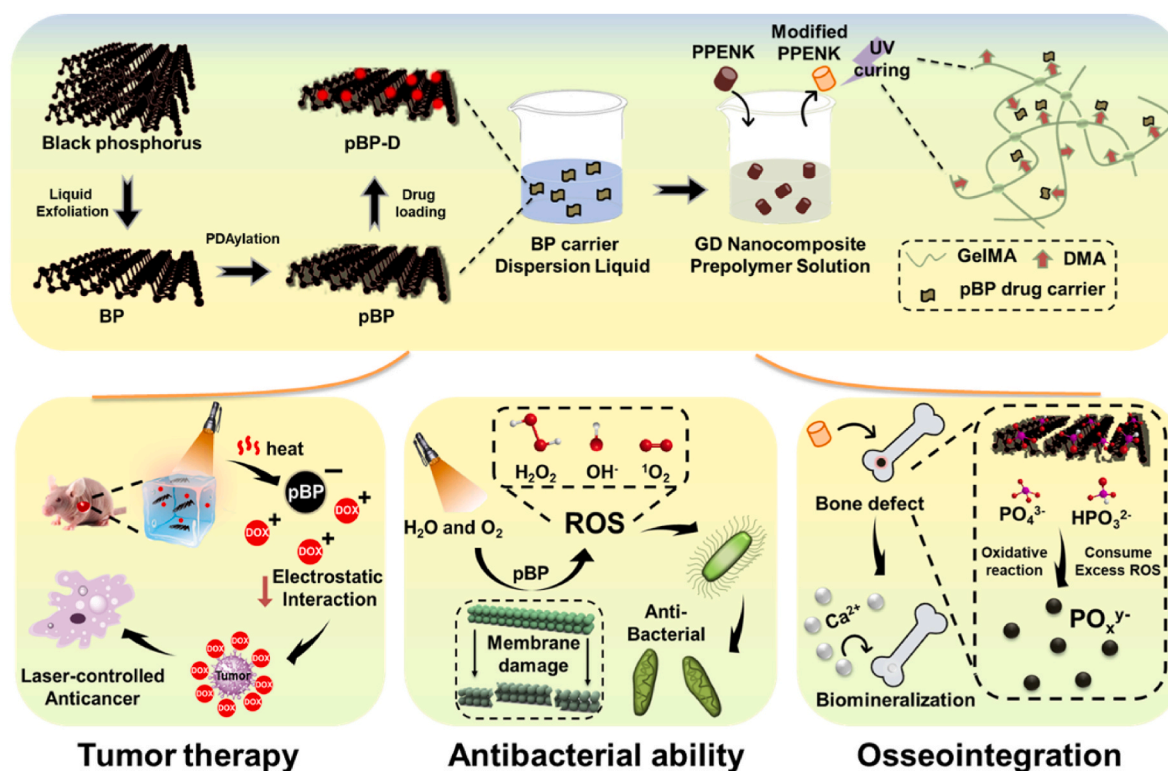

Fig. 1. Schematic diagram of the preparation of GelMA/DMA nanocomposite photo-crosslinking hydrogel coating on PPENK implant for tumor therapy, antibacterial infection and osseointegration.

be loaded with aggressive anticancer drugs such as doxorubicin hydro-chloride (DOX) via strong electrostatic interaction [7,8]. BP was regarded as a promising photothermal conversion agent for photothermal therapy (PTT) [[7,9,10]], which could not only control the release of drugs, but also eradicate bacteria through PTT-induced temperature rise [11]. In addition to PTT effect, BP was employed as photodynamic treatment (PDT) agent to produce reactive oxygen species (ROS) including superoxide anion radical, singlet oxygen, hydrogen peroxide and the highly reactive hydroxyl radical [12]. Owing to the cytotoxicity of ROS, PDT showed a wide range of antitumor and antibacterial bio-activities without the problem of drug resistance [13]. In addition, in contrast to other 2D materials like graphene [14–16], MXenes [17], BP could be easily degraded into harmless phosphate which showed supe-rior biocompatibility [18] and osteogenic differentiation. Interestingly, BP was also a promising ROS scavenger in the treatment of acute kidney injury [19] which could remove excess ROS in the absence of laser irradiation. Therefore, BP as effective antioxidative agents in vivo for therapy were expected to be explored. Although the prospect seemed encouraging, its practical applications were still quite challenging because the BP atomic layer degraded quickly when exposed to envi-ronmental conditions. Consequently, it was essential to exploit a modification method to enhance the stability of BP. Sun et al. [6] proposed polyethylene glycol-amine (PEG-NH$_2$) treated BP to enhance their biocompatibility and physiological stability. Xing et al. [20] believed that the coverage of BP with graphene oxide (GO) overcame the oxidation and instability issue of BP. However, most of these methods were not suited in the systems of drug delivery. Zeng et al. [21] demonstrated the modification of BP with polydopamine (PDA) to improve the stability and photothermal properties of bare BP. Due to the presence of functional groups in PDA, PDA/BP was also a possible ma-trix for proteins adsorption [22].

As a kind of high-performance polymer material, polyarylether ketone (PEEK) was regarded as one of the most promising biomaterials to replace metal materials for bone implants in the future. However, due

to the difficulty in processing PEEK materials and the low solubility, resulting in higher costs, there was an urgent need to find an alternative. Starting from the molecular structure design, our group [23] introduced a fully aromatic heterocyclic, non-coplanar structure of azanaphthalene biphenyls (DHPZ) into the polymer molecular chain and solved the conflict between high temperature resistance and solubility of tradi-tional high-performance resins. As a representative of new high-performance resin, poly(phthalazinone ether nitrile ketone) (PPENK) not only had similar mechanical strength to human bone, but was easy to process compared to PEEK. To further improve the biocompatibility of implants [24,25], some natural bio-macromolecular hydrogel was introduced [26]. Especially, gelatin, a hydrolyzed form of collagen, has got a lot of focus for its wide range of sources, biode-gradability, and superior sol-gel characteristics [27]. Gelatin for their potential to mimic characteristics of the extracellular matrix (ECM) environment has developed in native tissues [28]. In particular, gelatin modified with methacrylate (GelMA) to form hydrogels under UV light has been widely used as a bone repair material [29]. It was worth noting that the functionalization of bone implant materials was one of the necessary conditions to solve the complex situation, and also the key to the success of implantation. Especially in clinical application, bone defect caused by tumor resection and bacterial infection caused by traumatic injury required bone tissue engineering material to provide effective treatment. This made multifunctional bone implant materials more promising for clinical application [30].

Considering these factors, we designed and fabricated a mussel-inspired multifunctional photo crosslinking gelatin (GD) hydrogel coating containing nanoparticles on a bioinert PPENK substrate. GD hydrogel coating on the surface of PPENK could significantly improve the biocompatibility of PPENK, and th e adhesion of the coating was improved due to the introduction of catechol. To the best of our knowledge, it was the first demonstration that BP nanomaterials could simultaneously achieve multiple functions such as laser-controlled cancer for the treatment of cancer, preventing bacterial infection and

inducing regeneration of bone tissue. In particular, the BP was wrapped by PDA (pBP) to improve its stability and photothermal performance. In general, as shown in Fig. 1, we hypothesized that the mussel inspired GelMA hydrogel could perfectly accomplish the controllable drug release by 808 nm laser. At the same time, ROS produced by laser stimulation of pBP could destruct the cell membrane of bacteria, thus achieving antibacterial activity. More interestingly, in the long-term implantation process, pBP could also consume excess ROS, which could slowly degrade into PO_x^{y-}, and play an important role in osteogenesis. Our current results hypothesized that these merits would act in a cooperative manner to promote the osseointegration of PPENK implant even under tumorous and bacterial conditions, which may endow PPENK implants with excellent application prospects in therapy of complex bone defects. In the future, this nanocomposite multifunctional hydrogel coating could improve the performance of implant materials, thereby reducing the pain of patients.

2. Experimental

The following section summarized brief information on materials and methods used in this paper. More details have been described in the Supporting Information.

2.1. Materials

Poly (phthalzinone ether nitrile ketone) (PPENK) was purchased from Dalian Poly New Material Co., Ltd. (Dalian, China). Gelatin (Type A), Dopamine, 1-[4-(2-hyroxyethoxy)-phenyl]-2-hydroxy-2-methyl-1-propane-1-one (Irgacure 2959) and Methacrylic anhydride were purchased from Aladdin. Bulk BP crystal was purchased from MOPHOS technology Co., Ltd (Shenzhen, China). The other reagents were analytically pure and used as received.

2.2. Synthesis and characterization of GelMA and DMA

GelMA and DMA were synthesized as described previously with slight modification [31,32]. The synthesis details were shown in the Supporting Information. ^{1}H NMR spectra of GelMA and DMA were obtained on a Bruker DRX 400 NMR spectrometer (Bruker, Germany) with deuterium oxide or DMSO-d6 [33].

2.3. Synthesis and characterization of nano drug-loaded particles

N-methyl-2-pyrrolidone (NMP) [34], dimethyl sulfoxide (DMSO) [35,36], isopropanol (IPA) [10], even distilled water could lead to good exfoliation efficiency [37]. In this paper, we chose NMP solvent exfoliation technique [15] to prepare the BP nanosheets with high-yield production. The pBP and drug loaded nanoparticles (called BP-D or pBP-D) were fabricated according to a previously reported technique [7]. The morphology of nanoparticle was examined by using transmission electron microscopy (TEM) (Hitachi, Japan) and atomic force microscopy (AFM) (Bruker, Germany). The size and zeta potential were characterized by using a Zeta sizer Nano ZS90 (Malvern, UK). The chemical structure was examined by using DXR Laser Confocal Raman Microscope (Thermo Fisher, US), UV Spectrophotometer (Lambda 750S, US), and X-ray photoelectron spectroscopy (XPS) (Thermo Fisher, US). The supernatant after centrifugation of degraded BP or pBP was tested by Inductive Coupled Plasma Emission Spectrometer (ICP) (Perkinelmer, USA), and the mass of phosphate ions was calculated.

2.4. Preparation and characterization of nanocomposite hydrogel coatings

The PPENK substrates were obtained by the hot-pressing method and washed with ethyl alcohol, acetone, and deionized water for further used [38]. The GelMA/DMA hybrid solution which spin coated on the surface of PPENK was called GD/PPENK. The solution containing BP or pBP were called GD@BP/PPENK and GD@pBP/PPENK, respectively. The section morphology of hydrogel coatings was tested by SEM (SU-70, Hitachi, Japan). The adhesion ability of hydrogel coatings was tested by a 90°peeling tester (CRS/YN, Yanuo World Instrument Co. Ltd, China). To measure the ability of mineralization in vitro, all the samples were soaked in simulated body fluid (SBF) at 37 °C for 7 days [39].

2.5. Laser-controlled drug release and anticancer effect in vitro

In order to accurately calculate the drug release of hydrogel, block hydrogels were used instead of hydrogel coating in this part. The drug loading hydrogel without nanoparticles was called GD@DOX (DOX 1 mg/mL) and the hydrogels containing nanoparticles were called GD@BP-D and GD@pBP-D (BP or pBP 50 μg/mL, DOX 1 mg/mL), respectively. The photothermal properties were monitored by electronic thermometer under the irradiation of 808 nm NIR laser (KS–810F-8000) in PBS. The drug release was calculated by UV-VIS absorption spectrum. The antitumor effect was tested by MTT assay using HELA cells in vitro. In addition, the HELA cells co-cultured with different sample were stained with Calcein-AM/PI double stain kit (Yeasen, Shanghai) and Annexin V-Alexa Fluor 488/PI apoptosis detection kit (Yeasen, Shanghai) according to the instructions, respectively on day 7.

2.6. Photodynamic antibacterial activity in vitro

The photodynamic properties of BP and pBP were tested using an electron spin resonance spectrometer (EPR) (Bruker, E500, Germany) with 2,2,6,6-tetramethylpiperidine (TMPD) as the trapping agent for the detection of $^1O_2$ under dark or continuous laser irradiation (808 nm) for 10 min. 1,3-Diphenylisobenzofuran (DPBF) was a fluorescent probe with high specificity for $^1O_2$. It was used to detect the generation of ROS. The extracts of samples were tested by UV–vis measurement at different points [40].

E. coli (ATCC25922) and *S. aureus* (CMCC26033) were cultured in a common method and used until OD_{600}~0.5. The samples were cocultured with bacteria for one day [41], and the bacteria viability was determined by the standard plate-based counting method [42]. The bacteria were stained by Live/Dead Bacterial Staining Kit (Yeasen Biotech Co., Ltd., China). A confocal laser scanning microscope (CLSM, FV-1000, Olympus, Japan) was used to observe. The morphology of the bacteria was demonstrated by SEM.

2.7. Determination of cytocompatibility in vitro

MC3T3-E1 cells were seeded on different samples for a period time [43]. The cell viability was determined by MTT assay [44] and live/dead staining assay. For cell adhesion test, the cells were fixed, stained, and examined by laser scanning confocal microscope (CLMS) (Olympus, FV1000, Japan) [45].

2.8. Scavenging capability of pBP to consume ROS in vitro

In order to determine the antioxidative ability of BP nanoparticles in hydrogel coating, tBHP was used to induce oxidative stress. HUVEC cells were cocultured with different samples for 24 h, and DCFH-DA was used to test ROS level. A cell scratch experiment was used to test cell migration [46].

2.9. Osteo-differentiation studies in vitro

MC3T3-E1 cells were seeded on different samples for 7 and 14 days, osteogenic differentiation of MC3T3-E1 cells was evaluated to monitor the ALP activity [47], ARS deposition, Western blot and gene expressions of ALP, Col-1, RUNX2.
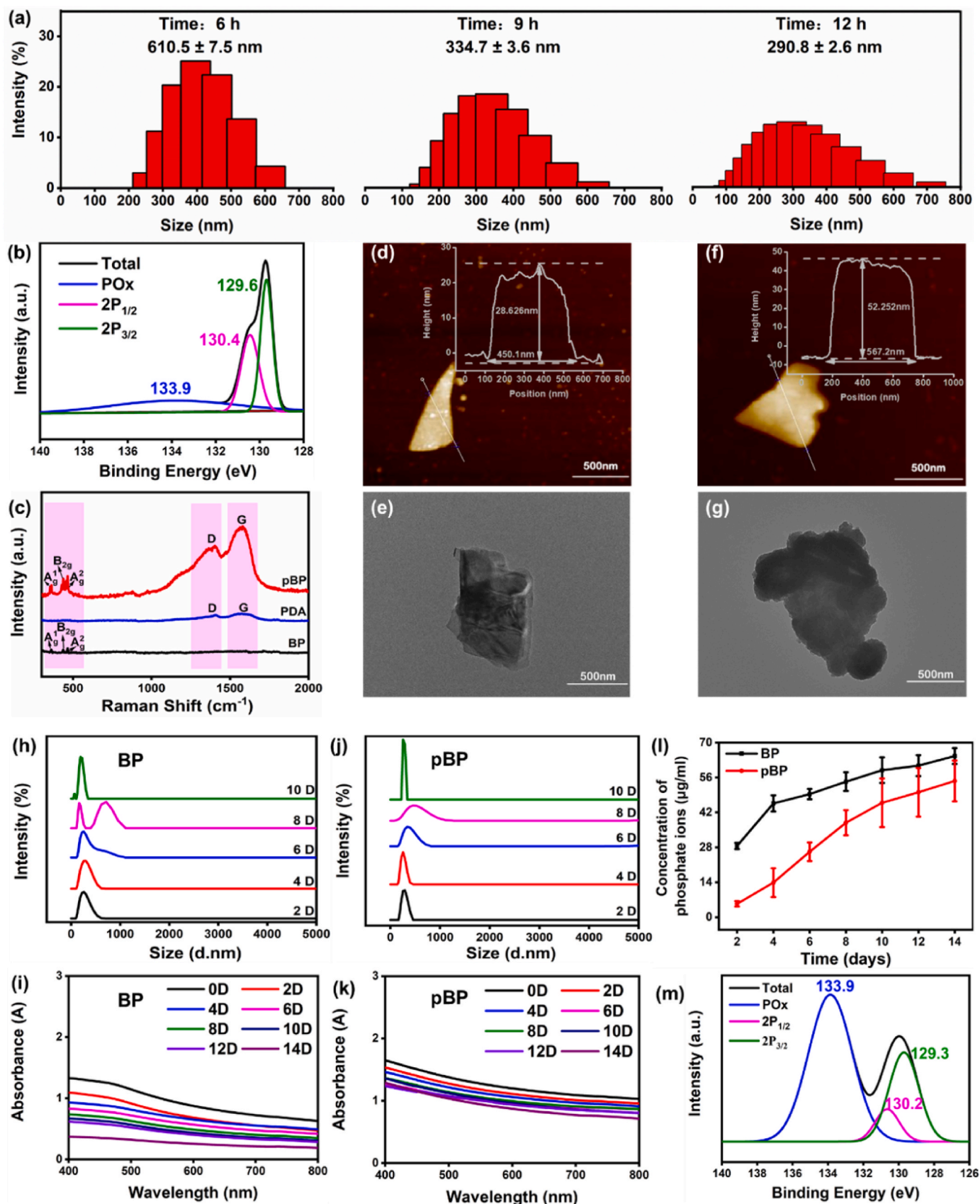
Fig. 2. Structural and morphology characterization of BP and pBP. (a) DLS of BP after exfoliation. (b) XPS spectrum of BP. (c) Raman spectra of BP, PDA and pBP. AFM images of (d) BP and (f) pBP (scale bar = 500 nm). TEM images of (e) BP and (g) pBP (scale bar = 500 nm). DLS of (h) BP and (j) pBP during degradation. UV–vis–NIR spectra of (i) BP and (k) pBP during degradation. (l) Concentration of phosphate ions determined by phosphomolybdenum blue method. (m) XPS of oxidized BP.

2.10. Antitumor model in vivo

The tumor model was built with HELA cells. Briefly, 100 μL of HELA cell suspension (1×10^7) was injected into the left axilla of each nude mouse (6 weeks). When the tumor volumes achieved about 90 mm³, mice (n = 3) were divided into four groups: (1) 100 μL of saline (negative control), (2) DOX@GD hydrogel (1 mg/mL DOX), (3) pBP-D@GD hydrogel (50 μg/mL pBP, 1 mg/mL DOX), (4) pBP-D@GD hydrogel (50 μg/mL pBP, 1 mg/mL DOX). All hydrogels were cut to the same size and filled around the tumor site. After suturing, group 4 was exposed to NIR laser (808 nm, 1W/cm², 10 min) on day 0, 2, 4, 8, 16 and 20. Tumor volume and body weight were also recorded. After 20 days, all mice were sacrificed, and representative heart, liver, spleen, lung, kidney, and tumor tissues were collected, fixed in 4% paraformaldehyde and blocked for histology analysis. The tissue samples were subsequently sectioned and stained with hematoxylin-eosin (H&E).

2.11. Osteogenic activity evaluation in vivo

Twenty-one Sprague-Dawley (SD) rats (6 weeks, 190–220 g) were randomly divided into three groups: (1) PPENK, (2) GD/PPENK, and (3) GD@pBP/PPENK. Before implantation, 10% pentobarbital sodium (0.3 mL/100 g) for anesthetization. An approximately 3 cm long, 3 cm diametral incision was made on SD rat femoral condyle. Then implants were implanted under an aseptic surgical environment. Lastly, these rats were executed at 5 and 10 weeks, and the harvested tissues with implants were immersed in 4% paraformaldehyde for further processing.

Micro-CT scanning (SCANCO, VivaCT 80, Switzerland) was used to measure new bone tissues around the implant. The surrounding area of implant with 4 mm radius was used for the quantitative analysis of new bone formation.

After evaluation of Micro-CT, the fixed bone tissue containing implants were dehydrated and embedded in polymethylmethacrylate for cutting hard tissue. Following that, the embedded tissues were processed into 60 μm slices for H&E, Masson and Giemsa staining. Femurs without implants (decalcified group) were decalcified with 10% EDTA (pH 7.4), dehydrated and embedded in paraffin. Then, 5 μm sections were cut for immunohistochemistry staining using primary antibodies against Col-1, Col-2 and OCN. After rinsing with PBS, the sections were incubated with secondary antibody at 37 °C for 30 min. Subsequently, the sections were stained with diaminobenzene, and cell nuclei were counterstained with hematoxylin. The positive expression was observed using a light microscope (Nikon, Japan).

2.12. Statistical analysis

All data were collected from at least three independent experiments. Statistical analyses were accomplished with SPSS statistic by comparing the mean values among samples using the one or two way (ANOVA) and Tukey's multiple comparison tests. Significant differences were statistically indicated by * P < 0.05, **P < 0.01. The results were exhibited as the mean value ± standard deviation.

3. Results and discussion

3.1. Preparation and characterization of materials for hydrogel

Methacrylate was used to modify the gelatin and dopamine for forming hydrogel under UV light. The ^{1}H NMR spectra of DMA and GelMA were dissolved in D$_2$O and DMSO-d$_6$ respectively as shown in Fig. S1 and Fig. S2. Additional peaks which were appeared in $\delta = 5{\sim}6$ ppm was the characteristic peaks of propylene. It is proved that we had prepared methacrylic anhydride modification of gelatin and dopamine successfully.

DMF, DMSO, IPA or ultrapure water could be used as solvent for liquid exfoliation. In this paper, a liquid exfoliation method with NMP as the solvent was used to prepare BP nanoparticles. The main reason was that NMP could effectively control the oxidation of BP during liquid exfoliation [48]. Besides, the thin layer of phosphorene with complete crystal structure and controllable dimension could be obtained by liquid exfoliation. Ultrasonic time determined the size of BP particle size, and the diameter distribution of BP measured by dynamic light scattering (DLS) spectroscopy was show in Fig. 2a. With the increase of ultrasonic time from 6 h to 12 h, the average particle size of BP decreased from 610.5 ± 7.5 nm to 290.8 ± 2.6 nm. To further explore the BP nanoparticles after ultrasound for 12 h, AFM and TEM were used to characterize its morphology as depicted in Fig. 2d–g. The BP nanoparticle had a 2D sheet-like morphology with lateral size of about 450 nm and thickness of about 28 nm. In contrast, after modification of PDA, the pBP nanoparticle had a larger size with 567.2 nm and a thicker thickness of 52.2 nm. Besides, the TEM of pBP showed that its surface was coved with particles, which probably be attributed to polydopamine. The chemical composition of the BP was shown in Fig. 2b. In the XPS spectrum, the BP showed the characteristic peaks of BP crystals with $2p^{3/2}$ and $2p^{1/2}$ doublets at 129.3 eV and 130.2 eV, respectively. In addition, the sub-band corresponding to oxidized phosphorus (PO$_x$) appeared at 133.9 eV but the peak intensity was weak, indicating BP could be well protected from oxidation in NMP solvent. In the Raman spectra of the BP and pBP in Fig. 2c, the three prominent peaks were attributed to A^{1}g at 360.7 cm^{-1} and B$_{2g}$ and A^2_g at 438.1 cm^{-1} and 466.9 cm^{-1}, respectively. The spectra of pBP not only exhibited the characteristic peaks of BP, but also the characteristic peaks of PDA which were attributed to D at 1403.2 cm^{-1} and G at 1581.6 cm^{-1}. The results showed that PDA was successfully modified on BP. Similarly, we performed XPS analysis on the chemical structure of pBP, and the result was shown in Fig. S3. Although the characteristic peak of phosphorus oxide appeared at 133.5eV, the intensity was not high, indicating that only a few amounts of BP was oxidized during the modification process, which would not affect the overall structure of the nanoparticles. Then, we tested the Zeta potential of BP before and after modification. The zeta potential of BP was −25mV, which was consistent with literature reports. The zeta potential of pBP was −48mV, which decreased relative to BP, due to the exposure of hydroxyl groups on the surface of polydopamine.

3.2. Degradation test

By utilizing the outstanding features of PDA, the biodegradation behavior of the BP and pBP in aqueous solutions was tested. The samples were kept in a shaker at 37 °C. As shown in Fig. 2h and j, the results of DLS indicated that BP had large particles agglomerated on days 8 and then small particles were detected on day 10, revealing that BP was degraded seriously. On the contrary, the particle size of pBP only fluctuated in a small range, investigating that pBP had good stability in a period time. The optical absorption band of BP showed that the absorption intensity decreased with extension of degradation time as shown in Fig. 2i. However, the absorption spectra of pBP shown in Fig. 2k exhibited a slight decrease. These results further demonstrated that PDA could protect BP and slow down its degradation rate. As for the implant materials used for bone regeneration, the capacity to produce a mineralized matrix was essential and could be simply evaluated in vitro by biomineralization [49]. The irreversible reaction with oxygen and water resulted in the degradation of BP to produce PO$_4^{3-}$ which was common byproducts in the human body [50,51]. Phosphomolybdenum blue method was used to detect the content of phosphate ions in the solution. As could be seen from Fig. 2l, the concentration of phosphate ions generated by degraded BP was slightly higher than that of pBP. Quantitative analysis of degraded BP and pBP was also performed by ICP, and the results were consistent with the data of phosphomolybdenum blue method as shown in Fig. S4. Meanwhile, XPS analysis was performed on its elemental composition as shown in Fig. 2m. Compared with Fig. 2b, the PO$_X$ peak at 133.9 eV was significantly enhanced,
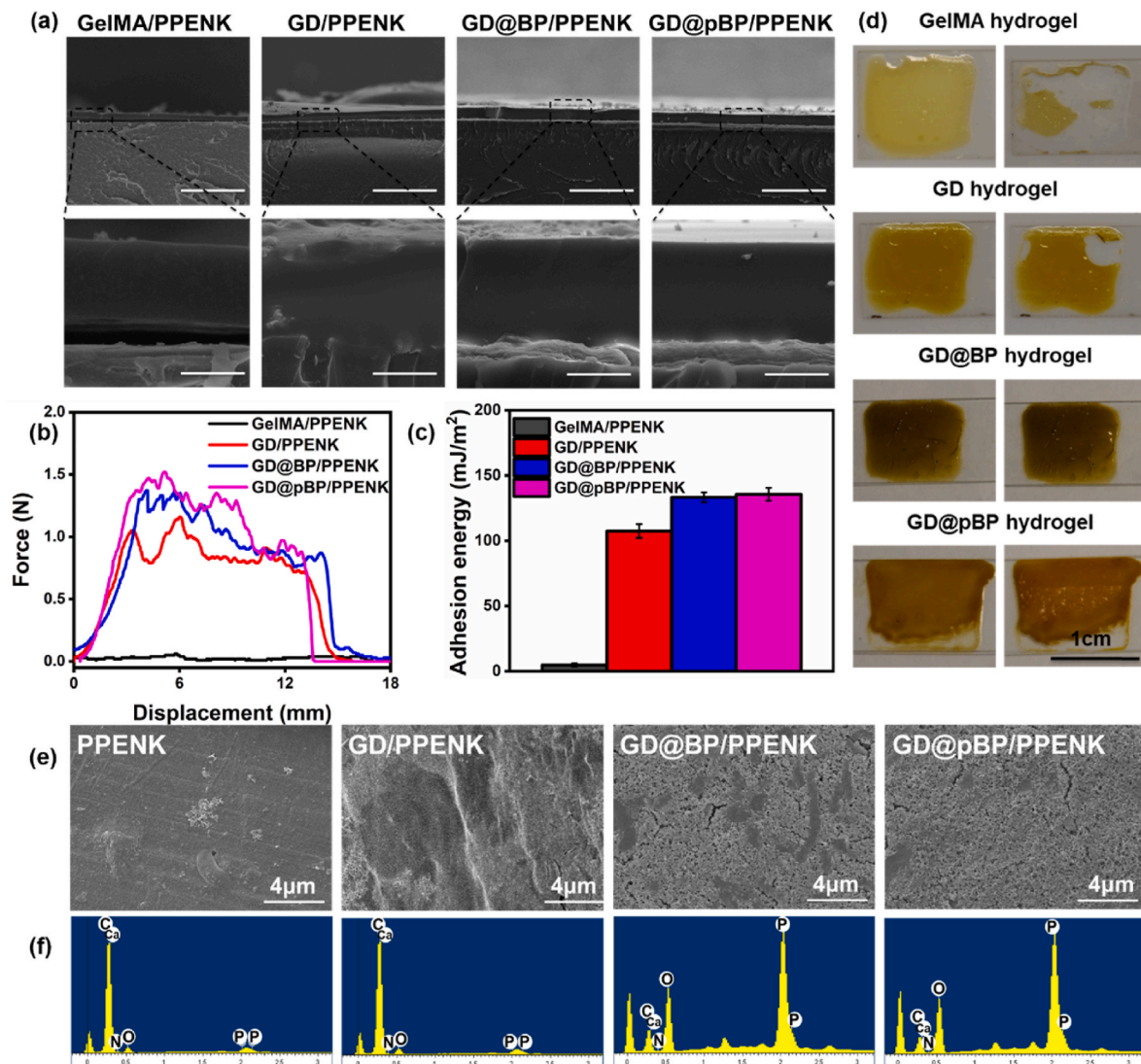
Fig. 3. Characterization of morphology, adhesion and in vitro mineralization of hydrogel coating. (a) SEM images of cross-sectional hydrogel coatings. Scale bar of top row: 200 μm. Scale bar of bottom row: 20 μm. (b) Force-displacement curves. (c) Peeling energy of different samples. (d) Adhesion test using 3 M adhesive tape. The left side represented the image before adhesion test and the right side represented the image after adhesion test. (e) SEM morphology images and (f) Energy Dispersive Spectroscopy (EDS) images of PPENK, GD/PPENK, GD@BP/PPENK and GD@pBP/PPENK after mineralization in SBF with 14 days.

indicating that BP or pBP was degraded into phosphate.

In order to measure the swelling and degradation ratios accurately, we prepared block hydrogels instead of hydrogel coating. As could be seen in Fig. S5, the swelling ratio of the GelMA hydrogel was the highest of 4.4 times. Due to the addition of DMA, the crosslinking density of GD hydrogel increased, and the swelling ratio of the hydrogel decreased a little. When combined with BP or pBP nanoparticles, the swelling ratio of the hydrogels did not change noticeably. To evaluate the degradation kinetics, the hydrogels were immersed in PBS solutions containing collagenase (2U/mL) at 37 °C and the loss masses were tested at various time points as shown in Fig. S6. For GelMA hydrogel, the mass loss was about 80% at day 3. In contrast, the remaining mass of GD hydrogel was only about 62% in two weeks. Besides, the addition of nanoparticles did not result in significant changes in degradation ratio. As a hydrogel coating on PPENK for implant material, the stable presence of the coating was an essential factor to enable that the loaded components could be delivered during the short-term recovery period after surgery [52].

3.3. Adhesion and biomineralization of nanocomposite hydrogel coating

Next, the hydrogel prepolymers were spin-coated and UV curing on the surface of PPENK substrates, and the cross-sectional morphology of hydrogel coatings was characterized by SEM as shown in Fig. 3a. The thicknesses of all coatings were about 30 μm. Apparently, there was no applied force between the GelMA hydrogel coating and the PPENK substrate (GelMA/PPENK), resulting in a gap. On the contrary, the other three hydrogel coatings containing DMA bound closely to PPENK substrate, indicating that the introduction of DMA greatly improved the adhesion ability of the coatings. In addition, due to the small size of BP nanoparticles, they could not be observed on the SEM image of the coating section. But in general, the addition of BP nanoparticles did not affect the adhesion properties of the coating. After that, a 90° peel test was performed to quantitatively evaluate the adhesion strength as could be seen in Fig. 3b. Compared with GelMA/PPENK, the tensile forces of the other three samples were significantly improved. The adhesion energy of GD@pBP/PPENK shown in Fig. 3c could reach 135.5 mJ/m². In order to show the adhesion performance of GD hydrogel more intuitively and clearly, we dripped the hydrogel coating on the glass instead of PPENK as shown in Fig. 3d. Obviously, the hydrogels containing DMA
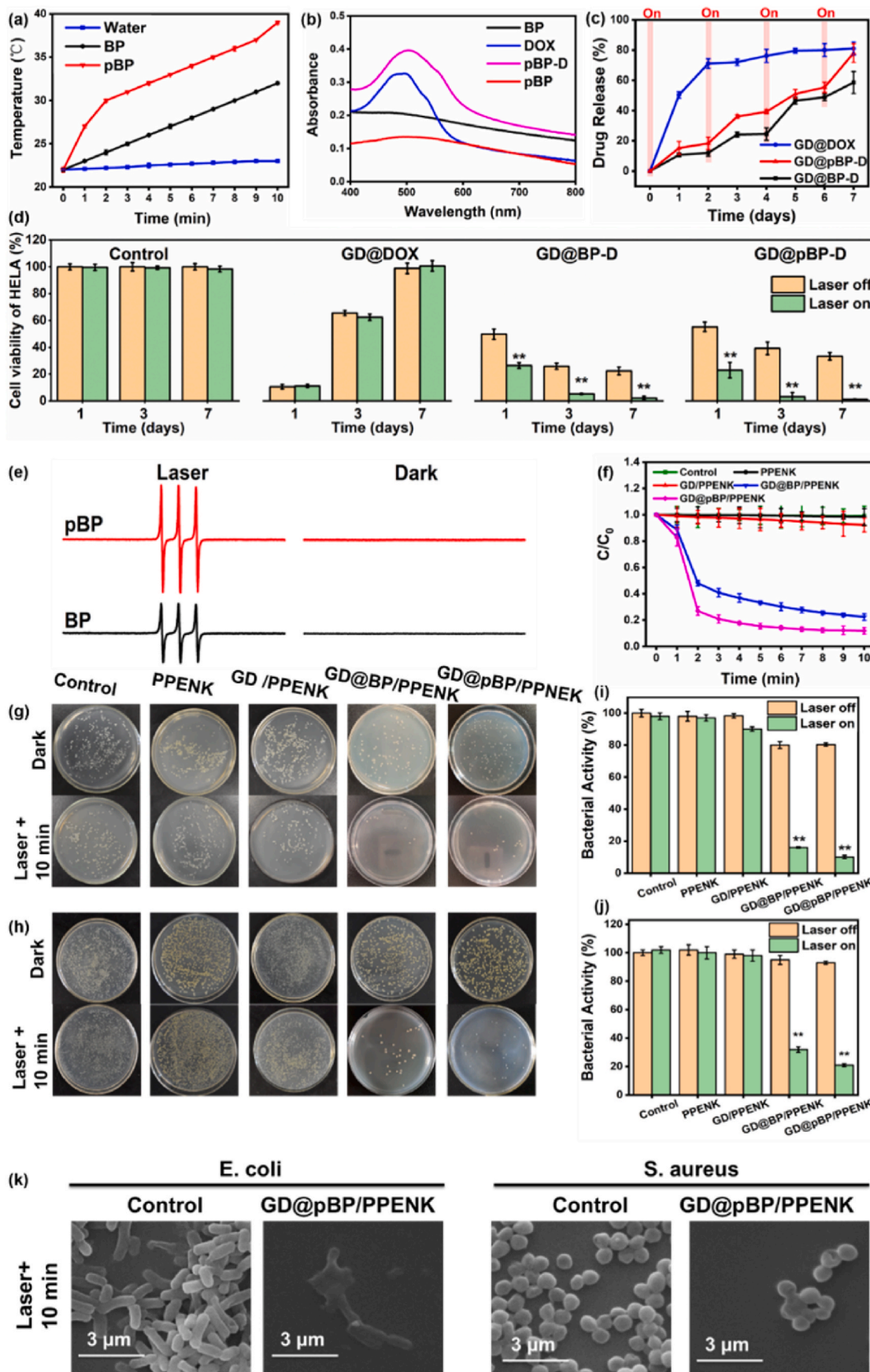
(caption on next page)

Fig. 4. Photothermal performance-controlled DOX release and PDT antibacterial performance in vitro. (a) Photothermal heating curves of pure water, BP and pBP irradiated with an NIR laser (808 nm, 1.0 W/cm^2) for 10 min. (b) UV–vis absorption spectra of DOX, BP, pBP and pBP-D. (c) Laser-controlled release of DOX from different samples in one weeks. (d) The relative cell viability of HELA cells incubated with different samples under laser off or laser on (808 nm, 1 W/cm^2, 10 min/day) for 1, 3 and 7 days. Laser on: turn on the laser and radiate the sample. laser off: turn off the laser. (e) EPR spectra of $^1O_2$ generated by BP and pBP under dark and laser stimulation. (f) Comparative trend of C/C_0 of DPBF under laser stimulation. C represented the OD value at different time, C_0 represented the initial OD value. Antibacterial performance of bacterial colonies against (g) *E. coli.* and (h) *S. aureus*. Bacterial activity of (i) *E. coli.* and (j) *S. aureus*. (k) Typical morphology of *E. coli.* and *S. aureus* incubated with GD@pBP/PPENK after laser irradiation.

adhered firmly to the glass surface, while GelMA hydrogel had widely broken. These results showed that the addition of DMA greatly improved the adhesion properties of the hydrogel coating and the nanoparticles did not affect its performance. It was mainly attributed to the Mytilus edulis foot protein 5 (Mefp-5) which could be self-assembled and deposited on the surface of any material [53].

It was well known that the released PO_4^{3-} could associate with Ca^{2+} to produce osteo-apatite in the bone tissue which could facilitate bone regeneration and osteointegration [18]. The nanocomposite hydrogels were then soaked in SBF solution for 14 days and evaluated by SEM as shown in Fig. 3e and f. On PPENK substrate, minerals were sparsely and randomly distributed, while on hydrogel, especially the hydrogel containing BP and pBP, the newly apatite nanoparticles were discovered and increased on the surface of hydrogels with BP. Although the protection of PDA delayed the degradation of BP, which resulting in a lower phosphate content, the ability of PDA itself to promote mineralization has been demonstrated. Therefore, GD@pBP/PPENK possessed the ability to facilitate mineralization in vitro under the synergistic effect of dopamine and BP in pBP.

3.4. In vitro laser-controlled antitumor and antibacterial activity

In order to evaluate the photothermal properties of BP, the aqueous solutions at 1.0 mg/ml were exposed to an 808 nm NIR laser at power density of 1.0 W/cm^2. The temperatures of water, BP and pBP aqueous solutions were measured for 10 min as shown in Fig. 4a. Pure water showed a negligible temperature change after irradiation. In sharp contrast, the photothermal efficiency of pBP ($\Delta T = 16.1$ °C) was improved compared to that of bare BP ($\Delta T = 9.8$ °C). The enhanced photothermal reaction of pBP may be attributed to the modification of PDA, which also had a strong photothermal conversion efficiency.

The drug loading of BP and pBP was determined to be about 400% tested by UV spectrophotometer. The nanoparticle loaded with drugs was characterized by UV–vis spectra as shown in Fig. 4b pBP-D displayed a slight red shift (from 480 nm to 503 nm) compared to free DOX. This redshift was similar to that of DOX loading on graphene [54], confirming the existence of an interplay between DOX and pBP. The XPS result of pBP-D shown in Fig. S7 showed that the structure of the nanoparticle was basically consistent with that of BP, indicating that no serious oxidation occurred during the preparation process. Afterwards, NIR laser at a wavelength of 808 nm was used to evaluate the photothermal effect of the embedded BP for drug release rate. The drug concentration released in the PBS solution (pH 7.4) was tested by UV–vis spectra. In order to accurately measure drug releasee, block hydrogels were used instead of hydrogel coating. The hydrogels containing DOX, BP-D and pBP-D were called GD@DOX, GD@BP-D and GD@pBP-D, respectively. The drug release of different samples without laser stimulation was first tested as shown in Fig. S8c. The drug release of GD@BP-D and GD@pBP-D was almost the same during 7 days, indicating that the nanoparticles had good absorption capacity of the drug. Then all samples were exposed to the NIR laser for 10 min (on) at 1, 3, 5 and 7 days and the rest of the time the laser was off. As shown in Fig. 4c, the release rate of GD@DOX was the fastest and it could not be controlled by laser. In the first two days, there was a trend of burst release. After three days, the amount of release was basically no longer increased. It was worth noting that the drug release of GD@BP-D and GD@pBP-D were controlled by laser stimulation. The drug release rates were reproducible within the first three consecutive on–off cycles. It

could be seen that the rate of laser on was much higher than rate of laser off, suggesting that BP and pBP could work as a potential optical switch of drug delivery. Importantly, the drug release of GD@pBP-D was the highest, probably attributed to the photothermal addition effect of PDA. The higher the temperature, the weaker the electrostatic attraction, so DOX could be released easier. In addition, considering the actual application environment was the acidic environment of the tumor, we used the same method to test drug release at pH = 5.0 as shown in Figs. S8a and S8b. The drug release trend was consistent with that at pH = 7.4 with or without laser stimulation. It was worth noting that, the release rate was increased at pH = 5.0, ascribed to the accelerated solubility of DOX at pH = 5.0, which was more conductive to the treatment of tumor.

To demonstrate that nanocomposite hydrogel coating had a controlled long-lasting sustained release antitumor effect, MTT assay of HELA cells we tested as shown in Fig. 4d. Observed from the control group, the laser clearly had little influence on cancer viability. Although the three-dimensional network of hydrogels could carry drugs and kill 80% of tumor cells, there was a disadvantage of burst release in group GD@DOX which could cause damage to normal cells. And once the tumor cells were not completely killed, they multiplied rapidly. In contrast, the addition of BP played a role in controlling drug release, and the pBP not only improved stability of BP, but also enhanced the photothermal efficiency of the carrier. The cell viability of the group of GD@BP-D and GD@pBP-D showed a big difference between laser on and off. In addition, the staining result of live/dead cells was shown in Fig. S9. Because of the burst release in the early stage that did not kill the cancer cells completely, HELA cells in the group of GD@DOX relapsed on day 7, so it showed a large number of living cells stained green on day 7. Under laser stimulation, large areas of red fluorescence appeared in the group of GD@BP-D and GD@pBP-D, indicating that cells have died. Without laser stimulation, only a few dead cells in the group of GD@BP-D and GD@pBP-D were stained in red. Cell apoptosis was further detected as shown in Fig. S10. The green fluorescence intensity of GD@pBP-D was the highest under laser stimulation, indicating that HELA cells in the group were in the early stage of apoptosis. Without laser stimulation, the fluorescence intensity of GD@pBP-D was weak, indicating that its anticancer effect on HELA cells was controlled by laser. Similarly, the GD@BP-D group had the same trend, but the effect was not as dramatic as GD@pBP-D. Since the group of GD@DOX did not have the capacity for long-term controlled drug release, HELA cells in this group were still proliferating on day 7, and only a few cells were in the early stage of apoptosis or died. Overall, GD@pBP-D had a long-term laser controlled antitumor effect.

Oxidative stress was one of the most common antibacterial mechanisms, which was mainly caused by the excessive accumulation of intracellular ROS, resulting in necrosis, apoptosis and death. As a light-responsive 2D nanomaterial, BP could convert light into heart or ROS to destroy bacteria under laser stimulation. In order to prove that ROS produced by photoexcitation was one of the antibacterial mechanisms of BP, EPR was used to explore the ability and type of ROS. As shown in Fig. 4e, there was no signal peak in both of them in the dark, indicating that BP and pBP did not produce $^1O_2$. In contrast, under laser irradiation for 10 min, both of them produced obvious $^1O_2$ characteristic signals, illustrating that illumination was one of the necessary conditions of BP to produce $^1O_2$, and the signal intensity of pBP was greater than that of BP. The formation of $^1O_2$ in the hydrogel coating could be further proved by degradation experiments of DPBF. In the presence of $^1O_2$, DPBF
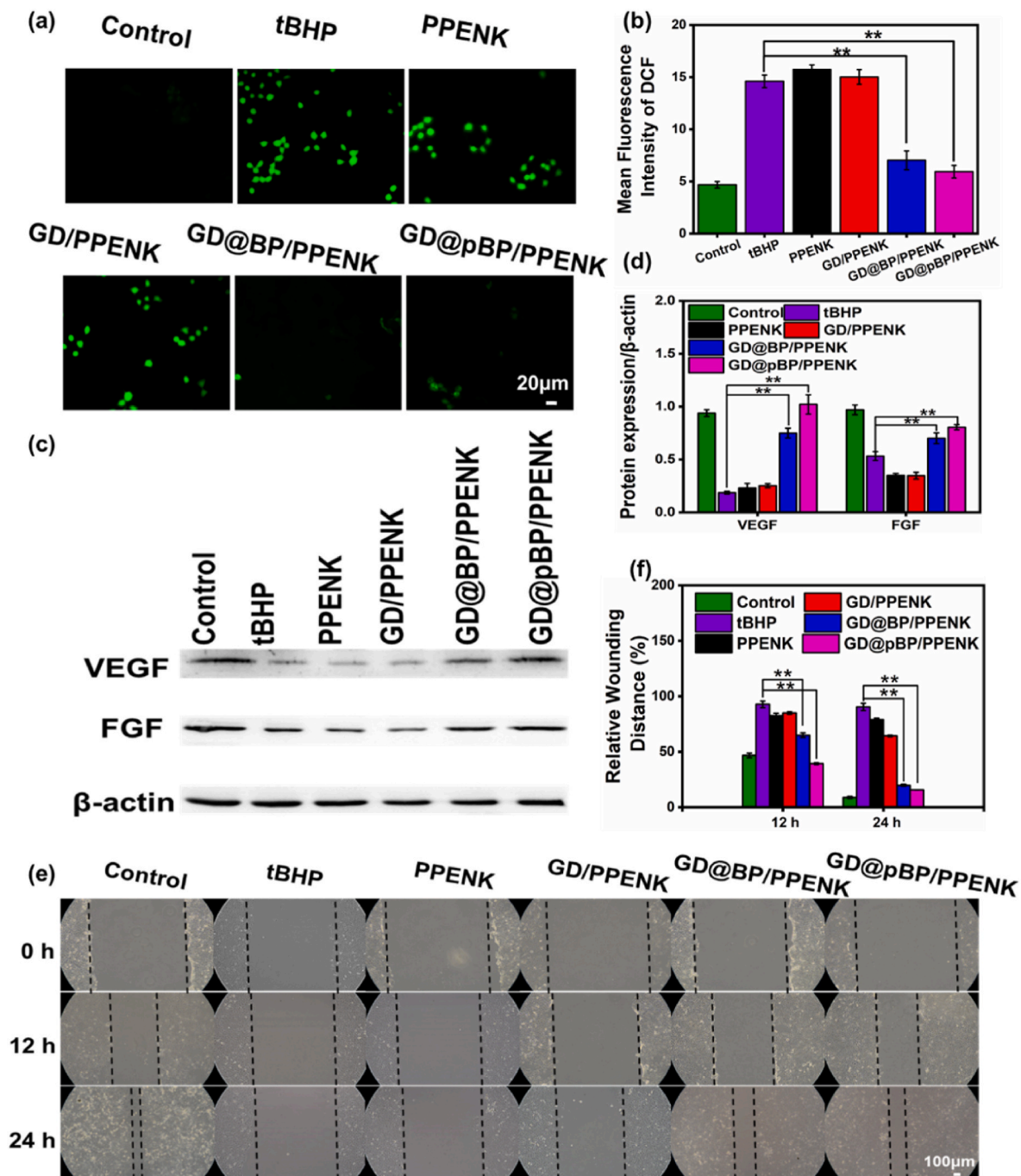
Fig. 5. ROS scavenging performance of GD@pBP/PPENK. (a) CLSM images of intracellular ROS level in HUVEC cells treated with different samples. Scale bar: 20 μm. (b) Quantification of mean fluorescence intensity of (a). (c) (d) Western blot detection and quantitative analysis of VEGF and FGF. (e) The image of wound healing in different samples at 12 h and 24 h. Scale bar: 100 μm. (f) Quantification of relative wounding distance.

would be oxidized and resulting in the decrease of the characteristic absorption peak at 410 nm. As shown in Fig. 4f, the absorbance of PPENK and GD/PPENK were almost the same as those of the control group when the four groups were stimulated by laser at the same time. It was indicated that $^1O_2$ would not be produced without BP. However, the absorbance of the GD@BP/PPENK and GD@pBP/PPENK were decreased significantly within 10 min and the degradation rate of GD@pBP/PPENK was up to 80%. So, the $^1O_2$ generation ability of BP and pBP under laser irradiation was proved again.

Subsequently, the general antibacterial properties were evaluated using *E. coli* and *S. aureus*. As could be seen in Fig. 4g and h, antibacterial activity against *E. coli* and *S. aureus* was assessed by spread plate

method. The number of the bacterial colonies on the GD@BP/PPENK and GD@pBP/PPENK groups with laser for 10 min NIR were much smaller than those of the GD/PPENK and PPENK control groups. From the quantitative results in Fig. 4i and j, it could be seen that GD@pBP/PPENK showed an antibacterial rate of 85% against *E. coli* and a slightly lower rate against *S. aureus*, but it could also kill more than 70% of *S. aureus*. The staining result of live/dead bacteria shown in Fig. S11 showed that after laser stimulation for 10 min, the red fluorescence intensity of dead bacteria in the GD@pBP/PPENK group was the highest, followed by GD@BP/PPENK. However, the group of PPENK and GD/PPENK showed green fluorescence of live bacteria, indicating that these two groups had no antibacterial effect under laser stimulation. To
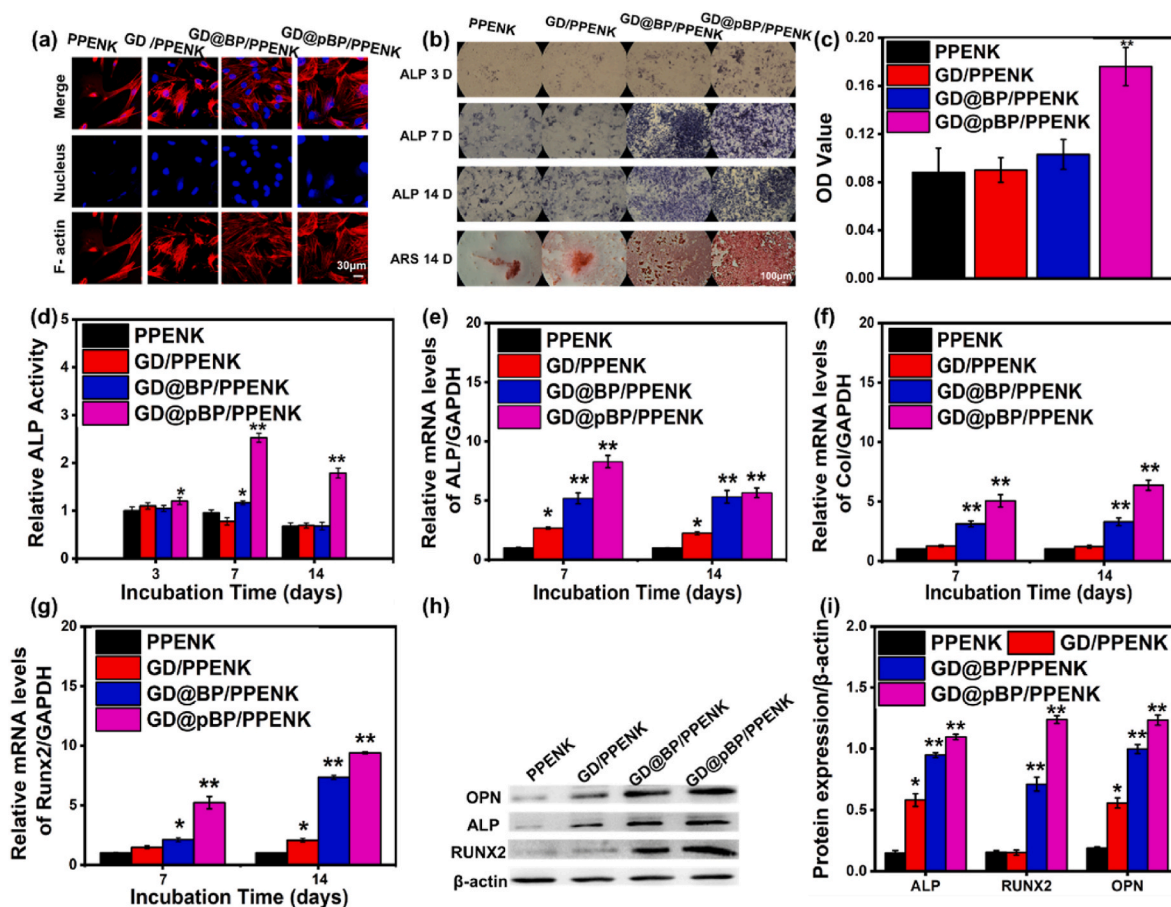
Fig. 6. Biocompatibility and osteogenic ability in vitro. (a) Fluorescence images of MC3T3-E1 cells stained with TRITC-phalloidin (red) and DAPI (blue) (scale bar, 30 μm). Osteogenic differentiation of MC3T3-E1 cells of (b) ALP staining on 3, 7 14 days and alizarin red staining on 21 days (scale bar, 100 μm). (c) Quantitative analysis of mineral deposition. (d) Relative ALP activity tested by BCA method. Gene expression of (e) ALP, (f) Col-1 and (g) RUNX2. (k) and (h) Western blot detection and (i) quantitative analysis of protein levels of OPN, ALP, and RUNX2 in each group.

further explore this antibacterial behavior, the morphology of *E. coli* and *S. aureus* on the surface of samples was observed by SEM. As shown in Fig. 4k, *E. coli* in the control group had the typical rod shape, *S. aureus* showed a full round structure. And the outer membrane of both bacteria was smooth and intact. However, after co-cultured with GD@pBP/PPENK, some bacteria in the two strains maintained the integrity of the membrane but most of the membrane was damaged, leading to the leakage of cell contents. These results indicated that GD@pBP/PPENK had a significant antibacterial effect against *E. coli* and *S. aureus*. ROS produced during PDT had a significant role in the destruction of bacterial cell membrane. This self-activating antibacterial effect solved the problems of conventional antibacterial agents inducing tissue toxicity or generating bacterial resistance due to continuous release of antibacterial agents [55]. Prevention of bacterial infections during the early implantation of bone implants was the key to shorten the recovery time of patients and improved the success rate.

3.5. In vitro antioxidant efficiency

Especially in the tumor microenvironment, the rate of ROS production was much higher than that of normal cells. Excess ROS were cytotoxic to cellular DNA which caused progressive oxidative damage and ultimately cell death [19]. Restriction of ROS was required for tumorigenesis [56]. Interestingly, BP was not only able to generate ROS under laser stimulation, but also acted as an antioxidant to effectively remove excess ROS ascribing to electron transfer induced by the layered structure [57]. Therefore, we tested the ROS levels in HUVECs under

oxidative stress conditions. As seen in Fig. 5a and b, the mean fluorescence intensity of PPENK and GD/PPENK increased significantly after treatment with tBHP compared with control group, mainly due to the oxidation of DCFH into fluorescent DCF by intracellular ROS. On the contrary, the green fluorescent signal declined when cells were pretreated with extracts of GD@BP/PPENK or GD@pBP/PPENK. We further conducted flow cytometry to quantitatively test ROS levels shown in Fig. S12. The relative ROS level in GD@pBP/PPENK group treated with tBHP reduced from 55.19% to 38.44%, indicating that GD@pBP/PPENK could act as oxidative protectors from excess ROS damage.

It was known that excess ROS could impede wound healing, which caused secondary damage in patients with bone defects [58]. The high migratory ability of HUVEC cells was an important factor for the formation of new blood vessels. A cell scratch was performed as shown in Fig. 5e. Under oxidative stress, the cell migration was remarkably inhibited. After coculturing with GD@BP/PPENK or GD@pBP/PPENK for 24 h, the scratches were recovered. Based on the relative wounding distance shown in Fig. 5f, the percentage of GD@pBP/PPENK was the lowest indicating that it acted as an excellent antioxidant. We further investigated the expression of VEGF and FGF by western blot as shown in Fig. 5c and d. The expression levels of VEGF and FGF were markedly decreased in the tBHP, PPENK and GD/PPENK compared with control group. Conversely, the expression levels increased in the GD@BP/PPENK and GD@pBP/PPENK groups. Even the expression level of VEGF in the GD@pBP/PPENK was higher than that in the control group. In summary, the synergistic effect of BP and PDA on
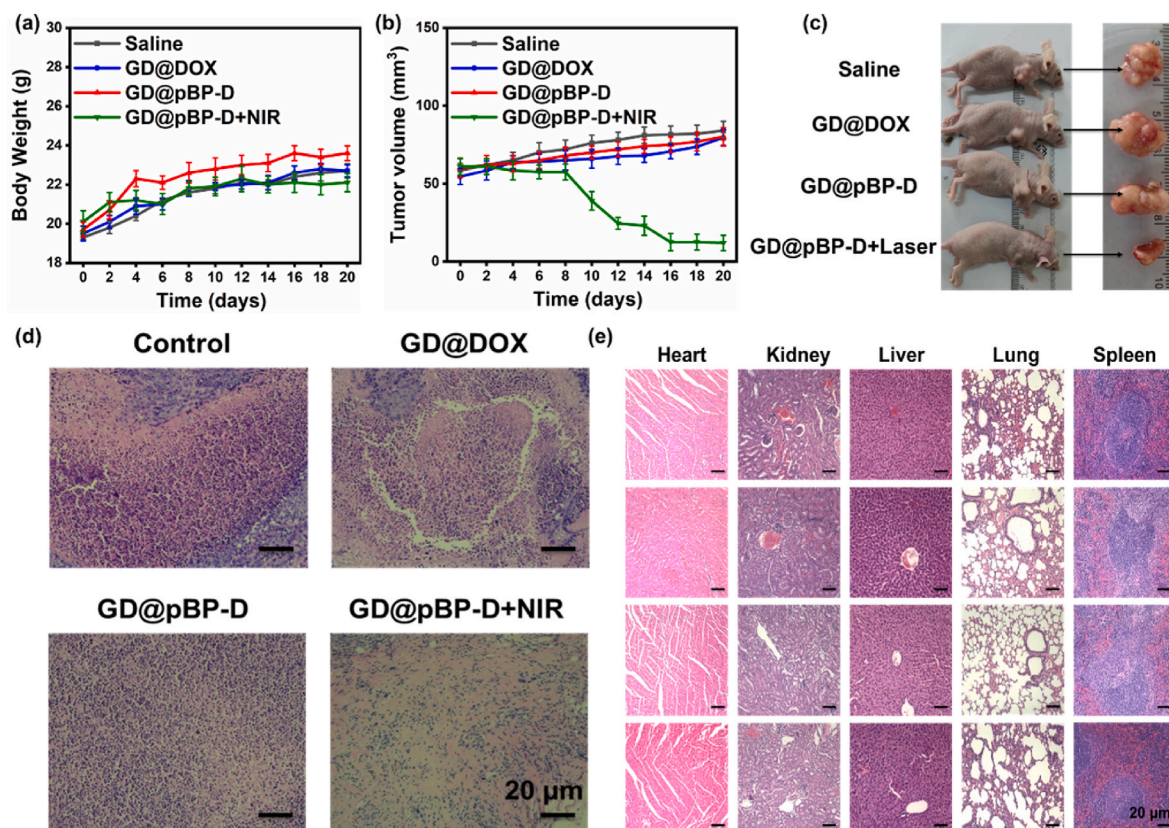
Fig. 7. The in vivo antitumor study. (a) Body weight of mice recorded every other day. (b) Corresponding growth curves of tumors in mice with different treatments. (c) Images of representative tumor in mice with different treatments. (d) Histological microscopy images of the tumor tissues stained with H&E after the treatments on day 21. Scale bar: 20 μm. (e) H&E-stained images of major organs from treated mice on day 21. Scale bar: 20 μm.

antioxidation made GD@pBP/PPENK as an ideal hydrogel coating to consume excess ROS in vitro.

3.6. In vitro cytocompatibility and osteogenic differentiation

Biosafety was an essential requirement for nanomaterials used in biomedicine. In order to explore the cytotoxicity of BP, MC3T3-E1 cells were cultured with 96-well plates containing different concentrations of BP for 1 day and 3 days, and the cell viabilities were tested by MTT assay. As depicted in Fig. S13, there was no obvious cytotoxicity even at a high concentration of 200 μg/mL, showing a potential biosafety of BP. We further investigated the cell viability of hydrogel coating on PPENK as shown in Figs. S14 and S15. Sample extracts were prepared according to ISO 10993. The extracts of the samples did not cause obvious cytotoxicity to MC3T3-E1 cells and cell viability was above 80%. Similarly, live/dead staining showed good biocompatibility and more cells stained in green were observed on the surface of GD@pBP/PPENK on day 3 as shown in Fig. S16. These results demonstrated that the modified surface of PPENK was nontoxic and suitable for cell proliferation. To further investigate the morphology of MC3T3-E1 on these substrates, the nucleus and cytoskeleton were stained using DAPI and FITC-phalloidin, respectively, and observed by confocal laser scanning microscopy as shown in Fig. 6a. After incubation for 24 h, the cells on PPENK were not well spread and their cytoskeleton was poorly developed. In contrast, the cells were significantly improved after modified by the hydrogel coating and the fluorescence intensity of F-actin in GD/PPENK, GD@BP/PPENK and GD@pBP/PPENK groups was higher than that of PPENK. And there were more lamellipodia on the surface of GD@BP/PPENK and GD@pBP/PPENK, indicating that the presence of BP and pBP could promote the cell adhesion and spreading.

It was well known that phosphate ions of degraded BP had the capture capacity toward calcium ions, which promoted biomineralization in a bone defect, thereby leading to excellent bone regeneration [49]. To verify the beneficial of BP containing hydrogels on osteogenic differentiation in vitro, the ALP activity and mRNA expression were carried out. As shown in Fig. 6d, the ALP activity of GD@pBP/PPENK was significantly elevated on day 7 and decreased on day 14, but the activity of GD@pBP/PPENK was still twice than that of PPENK substrate. Similarly, the results of PCR showed that expression of ALP genes, which was regarded as an early marker to provide energy for osteogenic differentiation, had the same trend as shown in Fig. 6e, f and 6g. Col-1 played a crucial function in the formation of the bone extracellular matrix. RUNX2 acted as an important transcription factor in osteogenic differentiation [49]. After 14 days, the expression of Col-1 and RUNX2 significantly enhanced co-cultured with PPENK modified by hydrogel coating. Remarkably, the level of GD@pBP/PPENK was the highest indicating that its excellent ability to promote mineralization in vitro played an important role in bone regeneration. We further performed ALP staining and alizarin red staining to show the ALP content and calcium deposition effect intuitively as shown in Fig. 6b and c. ALP stained in blue and calcium deposits stained in red could be seen clearly in the cells on GD@BP/PPENK and GD@pBP/PPENK rather than that on PPENK and GD/PPENK. Finally, western blot detection was used again to investigate the expression of ALP, OPN and RUNX2, the results were shown in Fig. 6h and i. GD@BP/PPENK and GD@pBP/PPENK could induce the expression of ALP, OPN and RUNX2 at the protein level. Compared with the other three groups, GD@pBP/PPENK could further up-regulate the molecular expression of genes related to osteogenesis, which was consistent with the results of PCR assay. The above data indicated that GD@pBP/PPENK had excellent osteogenic properties, mainly due to the release behavior of phosphate of pBP containing hydrogel coating and the synergistic effect of dopamine used to protect
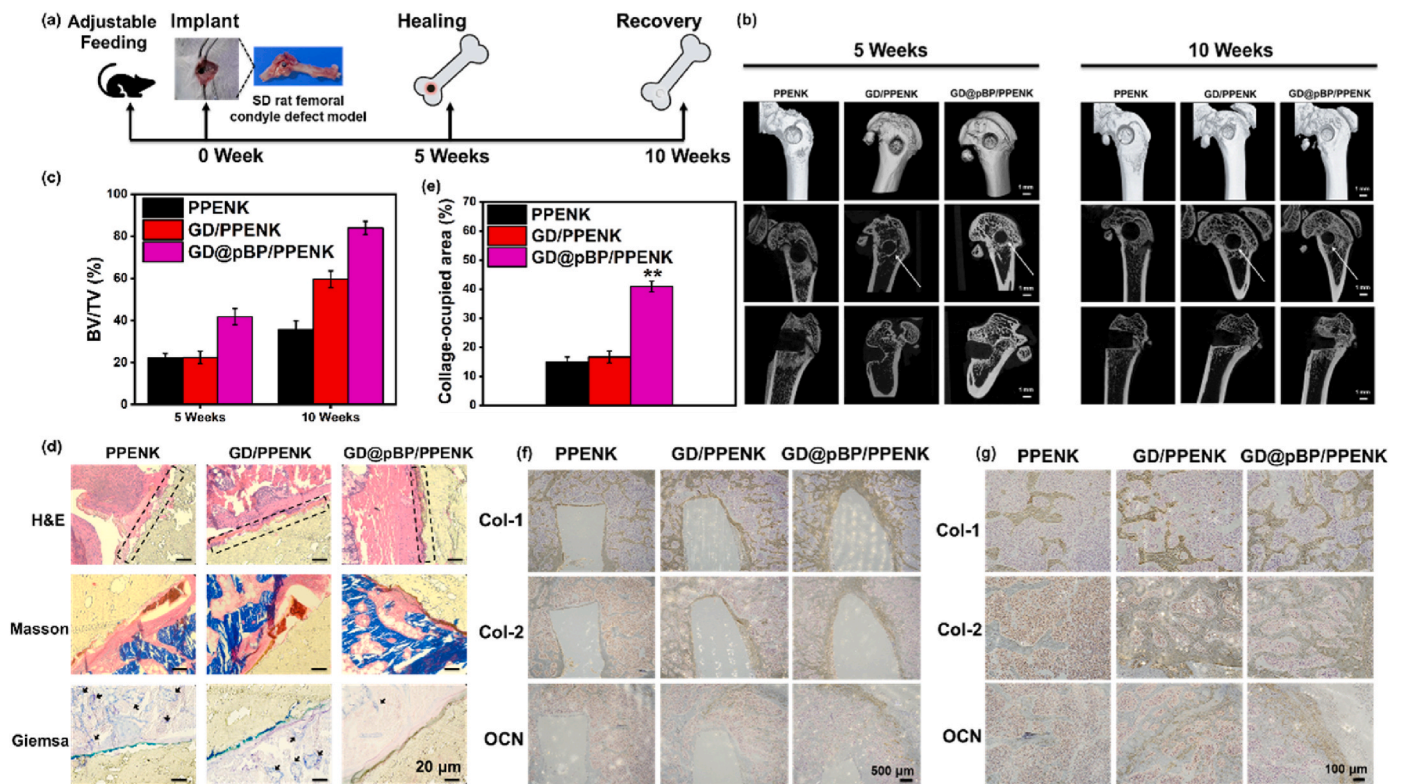
Fig. 8. Analysis of bone regeneration in vivo. (a) Overall timeline of bone healing. (b) Micro-CT images of femur defects showed different bone regeneration at 5 weeks and 10 weeks. (c) Quantitative analysis of bone volume to tissue volume (BV/TV) at 5 weeks and 10 weeks, n = 3 for each group. (d) Undecalcified histological analysis of H&E, Masson and Giemsa staining. Scale bar: 20 μm. (e) Quantitative analysis of collage-occupied area according to Masson staining. (f) Immunohistochemical analysis for bone regeneration of Col-1, Col-2 and OCN staining. Scale bar: 500 μm. (g) Magnified view of (f). Scale bar: 100 μm.

BP on mineralization. From the in vitro compatibility and osteogenesis test results, the material was expected to become a kind of excellent bone implantation material.

3.7. In vivo laser-controlled tumor eradication

With HeLa tumor-bearing mice as the research object, we studied the laser-controlled anticancer effect of GD@pBP-D hydrogel in vivo. In the section, we placed different hydrogel samples next to the tumor and intratumoral injection of saline was used as control group. Fig. 7a and b showed that the tumor volume of the GD@pBP-D + laser group was significantly reduced, while without laser stimulation, due to the electrostatic interaction between pBP and DOX, there was no tumor elimination effect in the group of GD@pBP-D. For the GD@DOX group, the drug had the problem of burst release, and because of the lack of carrier effect of pBP, its low drug loading was also the main reason for its inability to long-term anticancer. H&E staining analysis of tumors was also revealed that GD@pBP-D under 808 nm laser irradiation could efficiently kill the cells and induce apoptosis as shown in Fig. 7d. Obviously, within the 21-day treatment period, no weight loss in all mice and displayed a normally increased trend as shown in Fig. 7c. Moreover, the H&E staining analysis of the typical heart, kidney, liver, lung and spleen of the mice in Fig. 7e also showed no damage to normal organs [59,60]. In hence, the mussel-inspired gelatin hydrogels with or without the addition of pBP were of high biocompatibility and biosafety.

3.8. In vivo osteogenic evaluation

To explore long-term biocompatibility and osseointegration in vivo of PPENK modified by nanocomposite hydrogel coating, a SD rat femoral condyle defect model was established as shown in Fig. 8a. In this section, PPENK, GD/PPENK and GD@pBP/PPENK were implanted

separately and the condition of repair at 5 weeks and 10 weeks were determined. The micro-CT technology showed a 3D structure and 2D section of the newly formed bone around the implant as illustrated in Fig. 8b. A larger amount of new bone formation (shown by the white arrow) occurred on GD/PPENK and GD@pBP/PPENK group at 5 weeks than on control group at initial time. And much denser bone coverage was observed on GD@pBP/PPENK group compared with others. With increased implantation time, new bone tissue was hardly observed from PPENK group. In comparison, more newly formed tissue extended along the surface of GD@pBP/PPENK implant and filled the gap between implant and host bone. According to the quantitative analysis of new bone shown in Fig. 8c, the BV/TV values of GD@pBP/PPENK (41.81% ± 3.84 at 5 weeks and 83.96% ± 3.12 at 10 weeks) were higher than those of PPENK (22.07% ± 2.19 at 5 weeks and 35.74% ± 4.12 at 10 weeks) and GD/PPENK (22.41% ± 2.59 at 5 weeks and 59.64% ± 3.95 at 10 weeks). These results indicated that the GD@pBP/PPENK had the excellent capacity to facilitate bone tissue regeneration, which was consistent with osteogenic differentiation in vitro.

To confirm the above micro-CT results, the tissues containing the implants at 10 weeks postoperatively were further evaluated by H&E, Masson and Giemsa staining. As shown in Fig. 8d, H&E staining results showed that there were obvious cracks (black dashed box) around the pure PPENK implant, indicating that PPENK was not biocompatible. The other two groups of implants were more closely bound to the bone tissue and the tissue around the GD@pBP/PPENK implant was more regular and denser, indicating that it had good biocompatibility and the ability of bone regeneration. The load-displacement curves obtained from biomechanical tests of PPENK implants at 12 weeks were shown in Fig. S17. The bonding strength of the PPENK implant with surrounding bone was the lowest (F_{max} ~1.5 N). In comparison, the F_{max} of GD/PPENK implant was about 5 N, and the F_{max} of GD@pBP/PPENK implant increased significantly to ~10 N. The biomechanical test demonstrated

that the GD hydrogel coating containing pBP could enhance the bonding strength of PPENK with the surrounding bone. The fiber composition around the implant was assessed by Masson staining as shown in Fig. 8d. Collagen fibers produced by osteoblasts (stained in blue) were key to new bone formation. According to the quantitative result of Masson staining shown in Fig. 8e, the proportion of blue in GD@pBP/PPENK was the most, illustrating that its osteogenic effect was the best. In addition, Giemsa staining reflected that the GD@pBP/PPENK implant did not stimulate the animal to produce more neutral particles (black arrow). The above results showed that GD@pBP/PPENK was an excellent bone implant material compared with pure PPENK. Furthermore, we observed more Col-1, Col-2 and OCN positive staining areas in the GD@pBP/PPENK group as shown in Fig. 8f and g which supporting the osteogenesis in the long-term implantation. To verify the implantation effect of GD@pBP/PPENK again, the animal behavior analysis was tested at 0 week and 10 weeks after implantation as shown in Fig. S18. The front and back limbs of the rats were stained with ink, and their footprints were recorded as they crossed a track covered with white paper. The stride length and base length of GD@pBP/PPENK groups declined at 0 week after implantation caused by drilling during defect establishment. After implantation for 10 weeks, the base length returned to the normal level and the stride length was also closed to the health group. These results indicated that GD@pBP/PPENK was expected to become a kind of excellent bone implant material.

4. Conclusion

In summary, an adhesive, laser-controlled anticancer and antibacterial, ROS-scavenging, and osteogenic GelMA hydrogel coating was developed to modify the surface of PPENK. The multifunctional hydrogel coating was achieved by introducing pBP into UV-crosslinked GD network. The PDA modified BP could not only delay its degradation rate, but also improve the overall photothermal properties, which significantly improved the anticancer and PDT antibacterial effects under the control of laser. Moreover, in the process of long-term slow degradation in vivo, pBP could not only transform into PO_4^{3-}, which could repair bone defects, but also consume excess ROS and play an antioxidant role. Considering these results together, this work has exploited the enormous potential of pBP as promising photosensitizers for the treatment of cancer patients with bone defects. In the future, this technique can be used to treat patients with bone defects that have osteolysis problems caused by bone tumors. After implantation, the tumor can be effectively eliminated, while at the same time preventing postoperative bacterial infection. Most importantly, its excellent mineralization ability can promote the formation of new bone. This will greatly improve the cure rate of bone cancer patients.

Ethics approval and consent to participate

All animal experiments were approved by the Experimental Animal Ethics Committee of Dalian Medical University.

CRediT authorship contribution statement

Yizheng Li: Conceptualization, Methodology, Investigation, Writing – original draft, preparation. **Chengde Liu:** Supervision, Project administration, Funding acquisition. **Xitong Cheng:** Writing – review & editing. **Jinyan Wang:** Investigation. **Yue Pan:** Project administration. **Cheng Liu:** Project administration. **Shouhai Zhang:** Funding acquisition, Supervision. **Xigao Jian:** Supervision, and Project administration.

Declaration of competing interest

The authors declare that they have no known competing financial interests or personal relationships that could have appeared to influence the work reported in this paper.

Appendix A. Supplementary data

Supplementary data to this article can be found online at https://doi.org/10.1016/j.bioactmat.2023.04.020.

References

[1] J. Yin, Q. Han, J. Zhang, Y. Liu, X. Gan, K. Xie, L. Xie, Y. Deng, MXene-based hydrogels endow polyetheretherketone with effective osteogenicity and combined treatment of osteosarcoma and bacterial infection, ACS Appl. Mater. Interfaces 12 (2020) 45891–45903.

[2] A.L. Volsi, C. Scialabba, V. Vetri, G. Cavallaro, M. Licciardi, G. Giammona, Near-infrared light responsive folate targeted gold nanorods for combined photothermal-chemotherapy of osteosarcoma, ACS Appl. Mater. Interfaces 9 (2017) 14453–14469.

[3] W. Xi, V. Hegde, S.D. Zoller, H.Y. Park, C.M. Hart, T. Kondo, C.D. Hamad, Y. Hu, A.H. Loftin, D.O. Johansen, Z. Burke, S. Clarkson, C. Ishmael, K. Hori, Z. Mamouei, H. Okawa, I. Nishimura, N.M. Bernthal, T. Segura, Point-of-care antimicrobial coating protects orthopaedic implants from bacterial challenge, Nat. Commun. 12 (2021) 5473.

[4] C. Xing, S. Chen, M. Qiu, X. Liang, Q. Liu, Q. Zou, Z. Li, Z. Xie, D. Wang, B. Dong, L. Liu, D. Fan, H. Zhang, Conceptually novel black phosphorus/cellulose hydrogels as promising photothermal agents for effective cancer therapy, Adv. Healthc. Mater. 7 (2018), 1701510.

[5] D. Xiang, C. Han, J. Wu, S. Zhong, Y. Liu, J. Lin, X. Zhang, P.H. Wen, B. Özyilmaz, A.H.C. Neto, A.T.S. Wee, W. Chen, Surface transfer doping induced effective modulation on ambipolar characteristics of few-layer black phosphorus, Nat. Commun. 6 (2015) 6485.

[6] C. Sun, L. Wen, J. Zeng, Y. Wang, Q. Sun, L. Deng, C. Zhao, Z. Li, One-pot solventless preparation of PEGylated black phosphorus nanoparticles for photoacoustic imaging and photothermal therapy of cancer, Biomaterials 91 (2016) 81–89.

[7] W. Chen, J. Ouyang, H. Liu, M. Chen, K. Zeng, J. Sheng, Z. Liu, Y. Han, L. Wang, J. Li, L. Deng, Y. Liu, S. Guo, Black phosphorus nanosheet-based drug delivery system for synergistic photodynamic/photothermal/chemotherapy of cancer, Adv. Mater. 29 (2017), 1603864.

[8] J. Shao, H. Xie, H. Huang, Z. Li, Z. Sun, Y. Xu, Q. Xiao, X. Yu, Y. Zhao, H. Zhang, H. Wang, P.K. Chu, Biodegradable black phosphorus-based nanospheres for in vivo photothermal cancer therapy, Nat. Commun. 7 (2016), 12967.

[9] H. Cheng, X. Fan, E. Ye, H. Chen, J. Yang, L. Ke, M. You, M. Liu, Y.W. Zhang, Y. L. Wu, G. Liu, X.J. Loh, Z. Li, Dual tumor microenvironment remodeling by glucose-contained radical copolymer for MRI-guided photoimmunotherapy, Adv. Mater. 34 (2022), 2107674.

[10] W. Tao, X. Zhu, X. Yu, X. Zeng, Q. Xiao, X. Zhang, X. Ji, X. Wang, J. Shi, H. Zhang, L. Mei, Black phosphorus nanosheets as a robust delivery platform for cancer theranostics, Adv. Mater. 29 (2017), 1603276.

[11] Y. Deng, J. Shi, Y.K. Chan, D. Bai, R. Shu, X. Shi, Y. Li, L. Li, X. Yang, W. Yang, Heterostructured metal–organic frameworks/polydopamine coating endows polyetheretherketone implants with multimodal osteogenicity and photoswitchable disinfection, Adv. Healthc. Mater. 11 (2022), 2200641.

[12] Y. Zheng, A. Gao, J. Bai, Q. Liao, Y. Wu, W. Zhang, M. Guan, L. Tong, D. Geng, X. Zhao, P.K. Chu, H. Wang, A programmed surface on polyetheretherketone for sequentially dictating osteoimmunomodulation and bone regeneration to achieve ameliorative osseointegration under osteoporotic conditions, Bioact. Mater. 14 (2022) 364–376.

[13] B. Yuan, H. Wu, H. Wang, B. Tang, J.F. Xu, X. Zhang, A self-degradable supramolecular photosensitizer with high photodynamic therapeutic efficiency and improved safety, Angew. Chem. Int. Ed. 60 (2021) 706–710.

[14] H.Y. Mao, S. Laurent, W. Chen, O. Akhavan, M. Imani, A.A. Ashkarran, M. Mahmoudi, Graphene: promises, facts, opportunities, and challenges in nanomedicine, Chem. Rev. 113 (2013) 3407–3424.

[15] C. Xing, G. Jing, X. Li, E.D. Fan, Graphene oxide/black phosphorus nanoflakes aerogel with robust thermostability and significantly enhanced photothermal property in air, Nanoscale 9 (2017) 8035–8510.

[16] L. Chen, X. Zhong, X. Yi, M. Huang, P. Ning, T. Liu, C. Ge, Z. Chai, Z. Liu, K. Yang, Radionuclide 131I labeled reduced graphene oxide for nuclear imaging guided combined radio- and photothermal therapy of cancer, Biomaterials 66 (2015) 21–28.

[17] J. Xuan, Z. Wang, Y. Chen, D. Liang, L. Cheng, X. Yang, Z. Liu, R. Ma, T. Sasaki, F. Geng, Organic-base-driven intercalation and delamination for the production of functionalized titanium carbide nanosheets with superior photothermal therapeutic performance, Angew. Chem. Int. Ed. 128 (2016) 14789–14794.

[18] Y. Miao, X. Shi, Q. Li, L. Hao, L. Liu, X. Liu, Y. Chen, Y. Wang, Engineering natural matrices with black phosphorus nanosheets to generate multi-functional therapeutic nanocomposite hydrogels, Biomater. Sci. 7 (2019) 4046–4059.

[19] J. Hou, H. Wang, Z. Ge, T. Zuo, Q. Chen, X. Liu, S. Mou, C. Fan, Y. Xie, L. Wang, Treating acute kidney injury with antioxidative black phosphorus nanosheets, Nano Lett. 20 (2020) 1447–1454.

[20] C. Xing, G. Jing, X. Li, E.D. Fan, Graphene oxide/black phosphorus nanoflakes aerogel with robust thermostability and significantly enhanced photothermal property in air, Nanoscale 9 (2017) 8035–8510.

[21] X. Zeng, M. Luo, G. Liu, X. Wang, W. Tao, Y. Lin, X. Ji, L. Nie, L. Mei, Polydopamine-modified black phosphorous nanocapsule with enhanced stability and photothermal performance for tumor multimodal treatments, Adv. Sci. 5 (2018), 1800510.

[22] S. Ren, Y. Li, Q. Guo, Y. Peng, J. Bai, B. Ning, Z. Gao, Turn-on fluorometric immunosensor for diethylstilbestrol based on the use of air-stable polydopamine-functionalized black phosphorus and upconversion nanoparticles, Microchim. Acta 185 (2018) 429.

[23] S. Xiao, J. Wang, K. Jin, X. Jian, Q. Peng, Synthesis and characterization of a fluorinated phthalazinone monomer 4-(2-fluoro-4-hydroxyphenyl)-phthalazin-1 (2H)-one and its polymers from polycondensation reactions, Polymer 44 (2003) 7369–7376.

[24] L. Xie, G. Wang, Y. Wu, Q. Liao, S. Mo, X. Ren, L. Tong, W. Zhang, M. Guan, H. Pan, Pa K. Chu, H. Wang, Programmed surface on poly(aryl-ether-ether-ketone) initiating immune mediation and fulfilling bone regeneration sequentially, Innov 2 (2021) 100148.

[25] M. Li, J. Bai, H. Tao, L. Hao, W. Yin, X. Ren, A. Gao, N. Li, M. Wang, S. Fang, Y. Xu, L. Chen, H. Yang, H. Wang, G. Pan, D. Geng, Rational integration of defense and repair synergy on PEEK osteoimplants via biomimetic peptide clicking strategy, Bioact. Mater. 8 (2022) 309–324.

[26] L. Tong, Q. Liao, Y. Zhao, H. Huang, A. Gao, W. Zhang, X. Gao, W. Wei, M. Guan, P. K. Chu, H. Wang, Near-infrared light control of bone regeneration with biodegradable photothermal osteoimplant, Biomaterials 193 (2019) 1–11.

[27] J.S. Gonzalez, C. Mijangos, R. Hernandez, Polysaccharide coating of gelatin gels for controlled BSA release, Polymers 11 (2019) 702.

[28] Y. Zhang, R.K. Avery, Q. Vallmajo-Martin, A. Assmann, A. Vegh, A. Memic, B. D. Olsen, N. Annabi, A. Khademhosseini, A highly elastic and rapidly crosslinkable elastin-like polypeptide-based hydrogel for biomedical applications, Adv. Funct. Mater. 25 (2015) 4814–4826.

[29] Z. Zhao, G. Li, H. Ruan, K. Chen, Z. Cai, G. Lu, R. Li, L. Deng, M. Cai, W. Cui, Capturing magnesium ions via microfluidic hydrogel microspheres for promoting cancellous bone regeneration, ACS Nano 15 (2021) 13041–13054.

[30] G.L. Koons, M. Diba, A.G. Mikos, Materials design for bone-tissue engineering, Nat. Rev. Mater. 5 (2020) 584–603.

[31] J.W. Nichol, S.T. Koshy, H. Bae, C.M. Hwang, S. Yamanlar, A. Khademhosseini, Cell-laden microengineered gelatin methacrylate hydrogels, Biomaterials 31 (2010) 5536–5544.

[32] H. Lee, B.P. Lee, P.B. Messersmith, A reversible wet/dry adhesive inspired by mussels and geckos, Nature 448 (2007) 338–341.

[33] T. Seki, H. Kanbayashi, T. Nagao, S. Chono, M. Tomita, M. Hayashi, Y. Tabata, K. Morimoto, Effect of aminated gelatin on the nasal absorption of insulin in rats, Biol. Pharm. Bull. 28 (2005) 510–514.

[34] Z. Sun, H. Xie, S. Tang, X. Yu, Z. Guo, J. Shao, H. Zhang, H. Huang, H. Wang, P. K. Chu, Ultrasmall black phosphorus quantum dots: synthesis and use as photothermal agents, Angew. Chem. Int. Ed. 54 (2015) 11526–11530.

[35] H. Fu, Z. Li, H. Xie, Z. Sun, B. Wang, H. Huang, G. Han, H. Wang, P.K. Chu, X. Yu, Different-sized black phosphorus nanosheets with good cytocompatibility and high photothermal performance, RSC Adv. 7 (2017) 14618–14624.

[36] P. Yasaei, B. Kumar, T. Foroozan, C. Wang, M. Asadi, D. Tuschel, J.E. Indacochea, R.F. Klie, A.S. Khojin, High-quality black phosphorus atomic layers by liquid-phase exfoliation, Adv. Mater. 27 (2015) 1887–1892.

[37] H. Wang, X. Yang, W. Shao, S. Chen, J. Xie, X. Zhang, J. Wang, Y. Xie, Ultrathin black phosphorus nanosheets for efficient singlet oxygen generation, J. Am. Chem. Soc. 137 (2015) 11376–11382.

[38] X. Cheng, X. Yang, C. Liu, Y. Li, Y. Zhang, J. Wang, X. Zhang, X. Jian, Stabilization of apatite coatings on PPENK surfaces by mechanical interlocking to promote bioactivity and osseointegration in vivo, ACS Appl. Mater. Interfaces 15 (2023) 697–710.

[39] C. Liu, C. Liu, Y. Gao, F. Cheng, G.G. Xiao, J. Wang, X. Jian, Apatite Formation on poly (aryl ether sulfone ketone) surfaces by means of polydopamine layers functionalized with phosphonate groups, Adv. Mater. Interfac. 5 (2018), 1800003.

[40] Q. Ding, T. Sun, W. Su, X. Jing, B. Ye, Y. Su, L. Zeng, Y. Qu, X. Yang, Y. Wu, Z. Luo, X. Guo, Bioinspired multifunctional black phosphorus hydrogel with antibacterial and antioxidant properties: a stepwise countermeasure for diabetic skin wound healing, Adv. Healthc. Mater. 11 (2022), 2102791.

[41] W. Liu, C. Liu, C. Liu, Y. Li, L. Pan, J. Wang, X. Jian, Surface chemical modification of poly(phthalazinone ether nitrile ketone) through rhBMP-2 and antimicrobial peptide conjugation for enhanced osteogenic and antibacterial activities in vitro and in vivo, Chem. Eng. J. 424 (2021), 130321.

[42] J. Shao, C. Ruan, H. Xie, Z. Li, H. Wang, P.K. Chu, X. Yu, Black-phosphorus-incorporated hydrogel as a sprayable and biodegradable photothermal platform for postsurgical treatment of cancer, Adv. Sci. 5 (2018), 1700848.

[43] Y. Wu, Q. Liao, L. Wu, Y. Luo, W. Zhang, M. Guan, H. Pan, L. Tong, P.K. Chu, H. Wang, ZnL$_2$-BPs integrated bone scaffold under sequential photothermal mediation: a Win–Win strategy delivering antibacterial therapy and fostering osteogenesis thereafter, ACS Nano 15 (2021) 17854–17869.

[44] A. Gao, Q. Liao, L. Xie, G. Wang, W. Zhang, Y. Wu, P. Li, M. Guan, H. Pan, L. Tong, P.K. Chu, H. Wang, Tuning the surface immunomodulatory functions of polyetheretherketone for enhanced osseointegration, Biomaterials 230 (2020), 119642.

[45] S. Mo, F. Zhao, A. Gao, Y. Wu, Q. Liao, L. Xie, L. Tong, P.K. Chu, H. Wang, Simultaneous application of diamond-like carbon coating and surface amination on polyether ether ketone: towards superior mechanical performance and osseointegration, Smart Materials in Medicine 2 (2021) 219–228.

[46] Q. Chen, J. Li, F. Han, Q. Meng, H. Wang, Q. Wei, Z. Li, F. Li, E. Xie, X. Qin, S. Chen, W. Wang, C. Liu, B. Li, F. Han, A multifunctional composite hydrogel that rescues the ROS microenvironment and guides the immune response for repair of osteoporotic bone defects, Adv. Funct. Mater. 32 (2022), 2201067.

[47] J.B. Sun, Z. Wang, W. J, An, protection of icariin against hydrogen peroxide-induced MC3T3-E1 cell oxidative damage, Orthop. Surg. 13 (2021) 632–640.

[48] M. Zhu, Y. Osakada, S. Kim, M. Fujitsuka, T. Majima, Black phosphorus: a promising two dimensional visible and near-infrared-activated photocatalyst for hydrogen evolution, app, Catal. B 217 (2017) 285–292.

[49] K. Huang, J. Wu, Z. Gu, Black phosphorus hydrogel scaffolds enhance bone regeneration via a sustained supply of calcium-free phosphorus, ACS Appl. Mater. Interfaces 11 (2018) 2908–2916.

[50] W. Pan, C. Dai, Y. Li, Y. Yin, L. Gong, J.O. Machuki, Y. Yang, S. Qiu, K. Guo, F. Gao, PRP-chitosan thermoresponsive hydrogel combined with black phosphorus nanosheets as injectable biomaterial for biotherapy and phototherapy treatment of rheumatoid arthritis, Biomaterials 239 (2020), 119851.

[51] X. Wang, J. Shao, M.A.E. Raouf, H. Xie, H. Huang, H. Wang, P.K. Chu, X. Yu, Y. Yang, A.M. AbdEl-Aal, N.H.M. Mekkawy, R.J. Miron, Y. Zhang, Near-infrared light-triggered drug delivery system based on black phosphorus for in vivo bone regeneration, Biomaterials 179 (2018) 164–174.

[52] H. Cheng, K. Yue, M.K. Narbat, Y. Liu, A. Khalilpour, B. Li, Y.S. Zhang, N. Annabi, A. Khademhosseini, Mussel-inspired multifunctional hydrogel coating for prevention of infections and enhanced osteogenesis, ACS Appl. Mater. Interfaces 9 (2017) 11428–11439.

[53] H. Lee, S.M. Dellatore, W.M. Miller, P.B. Messersmith, Mussel-inspired surface chemistry for multifunctional coatings, Science 318 (2007) 426–430.

[54] H. Liu, T. Li, Y. Liu, G. Qin, X. Wang, T. Chen, Glucose-reduced graphene oxide with excellent biocompatibility and photothermal efficiency as well as drug loading, Nanoscale Res. Lett. 11 (2016) 211.

[55] J. Fu, W. Zhu, X. Liu, C. Liang, Y. Zheng, Z. Li, Y. Liang, D. Zheng, S. Zhu, Z. Cui, S. Wu, Self-activating anti-infection implant, Nat. Commun. 12 (2021) 6907.

[56] I.M. Reyes, N.S. Chandel, Cancer metabolism: Looking forward, Nat. Rev. Caner 21 (2021) 669–680.

[57] L. Wang, Y. Li, L. Zhao, Z. Qi, J. Gou, S. Zhang, J.Z. Zhang, Recent advances in ultrathin two-dimensional materials and biomedical applications for reactive oxygen species generation and scavenging, Nanoscale 12 (2020) 19516–19535.

[58] H. Zhao, J. Huang, Y. Li, X. Lv, H. Zhou, H. Wang, Y. Xu, C. Wang, J. Wang, Z. Liu, ROS-scavenging hydrogel to promote healing of bacteria infected diabetic wounds, Biomaterials 258 (2020), 120286.

[59] L. Zhou, W. Feng, Y. Mao, Y. Chen, X. Zhang, Nanoengineered sonosensitive platelets for synergistically augmented sonodynamic tumor therapy by glutamine deprivation and cascading thrombosis, bioact, Materials 24 (2023) 26–36.

[60] N. Zheng, Y. Fu, X. Liu, Z. Zhang, J. Wang, Q. Mei, X. Wang, G. Deng, J. Lu, J. Hu, Tumor microenvironment responsive self-cascade catalysis for synergistic chemo/chemodynamic therapy by multifunctional biomimetic nanozymes, J. Mater. Chem. B 10 (2022) 637–645.